Rare Metal Materials and Engineering
Volume
Available online at **www.rmme.ac.cn**

Cite this article as: Rare Metal Materials and Engineering,

Science Press

https://doi.org/10.12442/j.issn.1002-185X.20250625

Influence of Ce addition on the microstructure and mechanical properties of Al-Cu-Mn-Mg alloy

Wentao Yu[1,2], Han Zhang[3], Weixia Zhang[4], Yadong Lv[3], Haiyan Yang[3], Yanqing Xue[5], Qitang Hao[3]

[1] School of Mechanical and Material Engineering, Xi'an University, Xi'an 710065, China; [2] Shaanxi Key Laboratory of Surface Engineering and Remanufacturing, Xi'an University, Xi'an 710065, China; [3] State Key Laboratory of Solidification Processing, Northwestern Polytechnical University, Xi'an 710072, China; [4] TianCe Technology Co., Ltd., Xi'an, 710100, China; [5] Xi'an University of Posts and Telecommunications, Xi'an, 710121, China

Abstract: This study systematically investigated the influence of cerium (Ce) additions on the microstructure and mechanical properties of Al-Cu-Mn-Mg alloys through multi-scale characterization techniques including optical microscopy (OM), scanning electron microscopy (SEM), transmission electron microscopy (TEM), and X-ray diffraction (XRD). The results reveal that the addition of Ce leads to the formation of two distinct Ce-containing intermetallic compounds. The first is the primary $Al_{20}Ti_2Ce$ phase formed during solidification, which induces grain coarsening by consuming the effective grain-refining element Ti in the melt. The second Ce-containing phase is $Al_{16}Cu_4Mn_2Ce$, which forms through a eutectic reaction at the final stage of the solidification process. Unlike Al_2Cu, this phase is unstable at high temperatures and undergoes transformation into $Al_{24}Ce_3Cu_8Mn$ and $Al_{20}Cu_2Mn_3$ during heat treatment without dissolving. Consequently, it cannot contribute Cu and Mn to the Al matrix, resulting in a low degree of supersaturation. Furthermore, the minor addition of Ce retards the phase transformation from θ'' to θ' in the Al matrix. Thus, after identical heat treatment, the primary strengthening phase remains θ'' in the Ce-containing alloy, whereas it is θ' phase in the 0Ce alloy. These changes in the microstructure and phase composition directly degrade the mechanical properties of alloys: with Ce content increasing from 0 to 0.3wt.%, the ultimate tensile strength and yield strength decrease by 95 MPa and 45.5 MPa, respectively, and the elongation is reduced by about 50% compared to the 0Ce alloy.

Key words: Al-Cu-Mn-Mg alloy; Cerium; Microstructure; Mechanical properties

Al-Cu-based alloys are traditional heat-treatable materials used in the aerospace and automotive industries, owing to their properties of high strength, heat resistance and low density. Micro-alloying represents a pivotal strategy for further enhancing the mechanical performance of these alloys[1, 2]. In this context, rare earth (RE) elements have attracted considerable attention due to their profound influence on the microstructure and resultant properties of Al-Cu alloys[3-9]. The beneficial effects of RE additions are multifaceted, including melt purification, grain refinement, and modification of phase composition and precipitation behavior.

Among various RE elements, Ce has been the subject of extensive research as a promising micro-alloying candidate for Al-Cu alloys. However, reported findings on its role appear complex and sometimes contradictory, heavily dependent on the specific alloy system. For instance, Song et al.[10] reported that adding 0.45 wt.% Ce to an Al-Cu-Mg-Ag alloy markedly increased the nucleation density of the Ω phase by providing heterogeneous nucleation sites while also enhancing the thermal stability of Ω phase by impeding Cu atom diffusion. Li et

Received date:
Foundation item: Natural Science Basic Research Program of Shaanxi (No. 2024JC-YBMS-398); Scientific Research and Innovation Team of Xi'an University (No. 25WTCY05); Great Project of Ministry of Industrialization and Information of China (No. 2023ZY01010-06); China Postdoctoral Science Foundation (No. 2024MD753996)

Corresponding author: Yu Wentao, Ph. D., Senior lecturer, School of Mechanical and Material Engineering, Xi'an University, Xi'an 710065, P. R. China, E-mail: yuwentao417@xawl.edu.cn; Xue Yanqing, Ph. D., Associate Professor, Xi'an University of Posts and Telecommunications, Xi'an 710121, P. R. China, E-mail: xyq@xupt.edu.cn

al.[11] observed that introducing 0.25 wt.% Ce into a similar alloy led to the formation of Al_8Cu_4Ce phase during solidification, which resulted in a decrease in ultimate tensile strength and yield stress. Xiao et al.[12, 13] demonstrated that trace Ce additions could refine grain structure and promote a finer, denser distribution of Ω and θ' precipitates. However, they also noted that the co-addition Ce and Ti resulted in the formation of $Al_xTi_6Ce_3Cu$ compounds, causing grain coarsening and a reduction in tensile strength compared to alloys containing only Ce or Ti.

These conflicting reports underscore the fact that a definitive consensus regarding the role of Ce in Al-Cu alloys has yet to emerge, as its impact is intricately linked to the base composition[14-16]. Al-Cu-Mn-Mg alloys, as promising heat-resistant aluminum materials, have attracted considerable attention in recent years[2, 17, 18]. Therefore, this study systematically investigates the influence of Ce micro-alloying on an Al-Cu-Mn-Mg alloy. The objectives are to elucidate the underlying mechanisms governing microstructural evolution and to establish a clear correlation between Ce-induced microstructural changes and the resultant mechanical properties.

1 Experiment

The nominal compositions (wt.%) of the studied alloys are listed in Table 1. These alloys were fabricated using high-purity aluminum (99.99%), industrial-grade pure magnesium, Al-50Cu, Al-10Mn, Al-10Ce and Al-5Ti-1B master alloys. All raw materials were thoroughly cleaned to remove surface contaminants such as dust, oils, moisture, and corrosive residues. High-purity aluminum, along with the Al-50Cu, Al-10Mn, Al-10Ce intermediate alloys, was sequentially charged into a crucible placed inside a resistance furnace. The melt temperature was continuously monitored using a calibrated handheld thermometer. When the temperature of melt reached 700±5 ℃, industrial pure Mg was carefully introduced using a bell jar plunger, followed by stirring for 3-5 minutes to ensure homogeneous distribution of alloying elements. The melt temperature was then adjusted to 740-750 ℃, after which the inoculant (Al-5Ti-1B) was added and manually stirred for 5-10 minutes. Subsequently, the temperature was adjusted to 730-740 ℃, and the melt was refined using non-toxic refining agent (HGJ-1A). After refining, the melt was held for 10-20 minutes to allow for slag separation, after which the surface slag was removed. Once the alloy melt temperature stabilized at 720 ℃, it was poured into a preheated metal mold to obtain the experimental casting. Heat treatment was conducted in a muffle furnace. The samples were solutionized at 525 ℃ for 12 h, water quenched, and then aged at 175 ℃ for 6 h to obtain high number density of strengthening precipitates.

The phase composition of alloys was determined by X-ray diffraction (XRD, X'Pert PRO) with a scanning speed of 10°/min in the 2θ range of 10° to 90°. Samples for microstructure analysis were prepared using standard metallographic methods. Microstructures were characterized using an optical microscope (OM, GX-71) and a scanning electron microscope (SEM, FEI G3 UC). The chemical composition of secondary phases was analyzed using an energy-dispersive spectrometer (EDS) attached to SEM and transmission electron microscopy (TEM, JEM-2100F). Phase structures were further identified using selected area electron diffraction (SAED). Thin foils for TEM were prepared by cutting 3 mm disks, grinding them to approximately 50 μm in thickness, and final thinning by ion beam milling. Tensile tests were conducted on a WDW-50D microcomputer-controlled electronic universal testing machine at a crosshead speed of 2 mm/min. The Vickers hardness was measured using a microhardness tester (LM248AT, LECO, USA) under a load of 200 g (HV 0.2) with a dwell time of 15 s. At least ten indentations were made for each sample condition, and the results were averaged.

Table 1 Chemical composition of experimental alloy (wt fraction, %)

Alloys	Cu	Mn	Mg	Ti	Ce	Al
0Ce	5.0	1.0	0.35	0.3	0	Bal.
0.1Ce	5.0	1.0	0.35	0.3	0.1	Bal.
0.2Ce	5.0	1.0	0.35	0.3	0.2	Bal.
0.3Ce	5.0	1.0	0.35	0.3	0.3	Bal.

2 Results and discussion

2.1 Microstructure of the as-cast alloys

Fig. 1 presents the microstructural evolution of Al-Cu-Mn-Mg alloys with varying Ce additions. The average grain size, quantified using ImageJ software, The results indicate that the average grain sizes are 136 ± 15 μm, 214 ± 24 μm, 231 ± 20 μm, and 326 ± 48 μm for the alloys with 0Ce, 0.1Ce, 0.2Ce and 0.3Ce, respectively, demonstrating that Ce addition promotes grain coarsening. Concurrently, new secondary phases emerge with increasing Ce content. As shown in Fig. 1(c1)-Fig. 1(d2), two distinct types of secondary phase particles are present in the 0.2Ce and 0.3Ce alloys. One is the light-gray blocky/needle-like phase (indicated by yellow arrows in Fig. 1) with well-defined geometric boundaries, predominantly distributed within α-Al grains. The other is black strip-like phase distributed at the grain boundaries (indicated by red arrows in Fig. 1). Additionally, the microstructure shown in Fig. 1(b2) indicates that black strip-like particles also form in the 0.1Ce alloy, and the light-gray secondary phase can not be observed in this alloy. When the Ce content increases to 0.2 wt.%, gray blocky/needle-like particles begin to form within the *α*-Al grain.

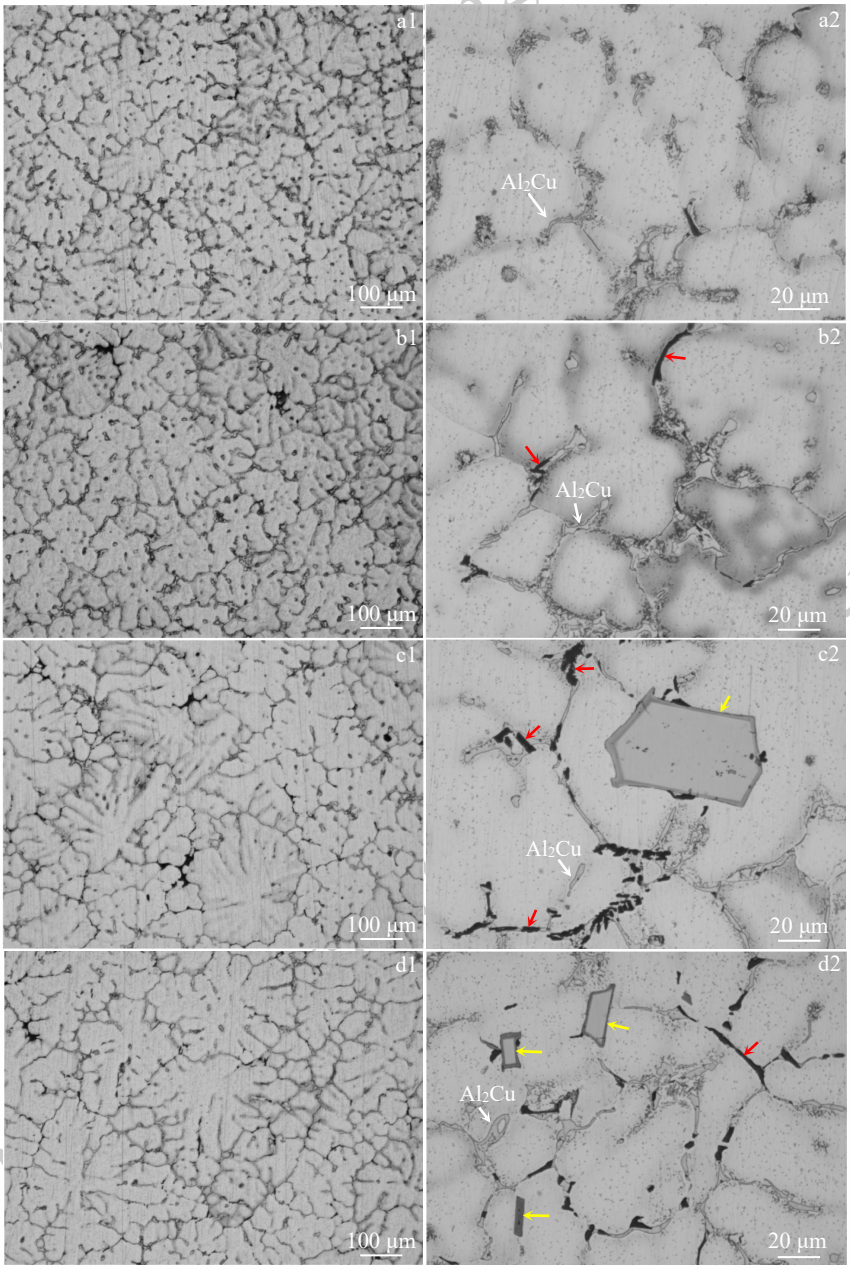

Fig. 1 Optical microscope images of as-cast alloys: (a1)、(a2) 0Ce alloy; (b1)、(b2) 0.1Ce alloy; (c1)、(c2) 0.2Ce alloy; (d1)、(d2) 0.3Ce alloy. The arrows with different colors indicate different phases

2.2 Phase composition

The XRD patterns of the as-cast alloys with different Ce contents are presented in Fig. 2. All samples consist primarily of α-Al and Al2Cu phases. For the higher-Ce alloys (0.2Ce and 0.3Ce), an additional single diffraction peak appears at 2θ ≈ 37.3°, indicating the formation of a new secondary phase. However, due to its low volume fraction, this phase cannot be conclusively identified by XRD and is therefore marked as "X" in the figure.

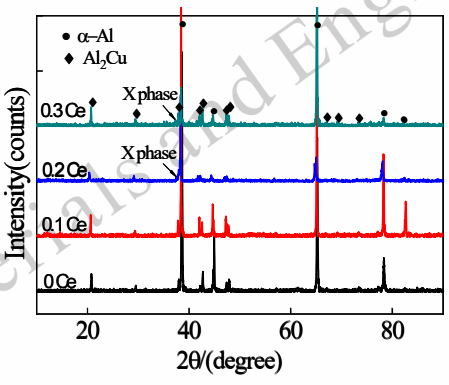

Fig. 2 XRD patterns of as-cast Al-Cu-Mn-Mg alloys with different Ce

contents

To identify the two types of secondary phases observed by OM, the 0.2Ce alloy and 0.3Ce alloy were further analyzed using SEM, TEM and EDS. As shown in Fig. 3, the phases within the grains exhibit polygonal and needle-like morphologies, characteristic of primary phases formed during solidification, with sizes reaching ~40 μm and ~150 μm, respectively. EDS analysis reveals that these block/needle-like phases are rich in Ti and Ce, along with minor amounts of Cu, Mg and Mn. The atomic ratio of Al, Ti, and Ce is approximate to 20:2:1, confirming the phase as $Al_{20}Ti_2Ce$. This compound forms by consuming Ti from the melt, which explains the observed grain coarsening (Fig. 1), as the Ti originally introduced for grain refinement is effectively depleted.

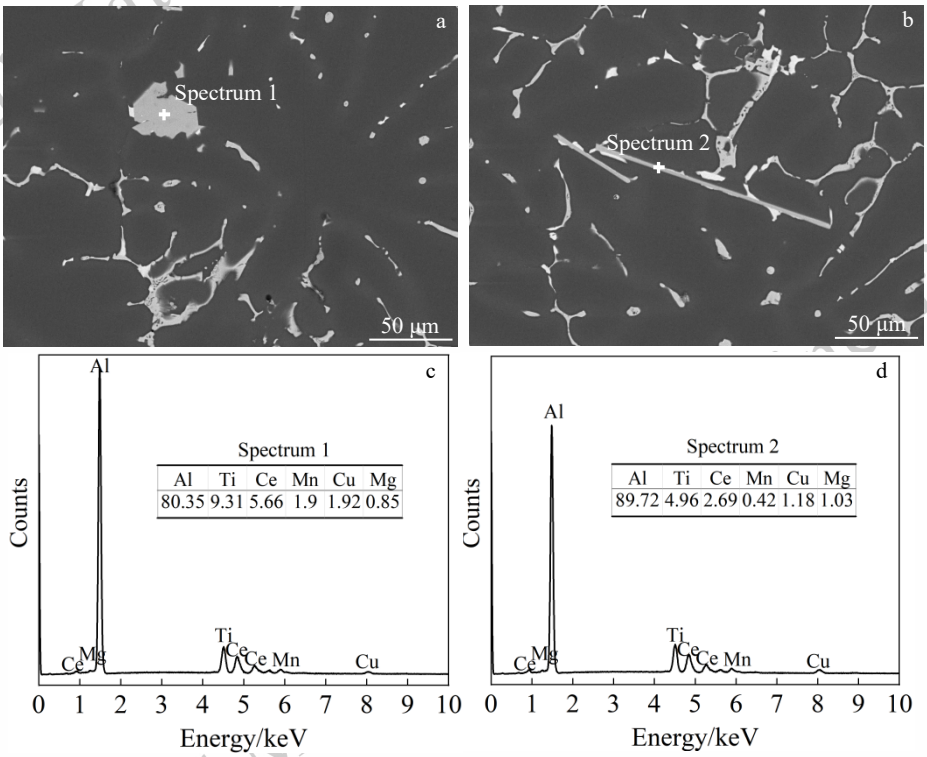

Fig. 3 Typical second phase in the Al matrix of as-cast 0.3Ce alloy: (a), (b) back-scattered electron images; (c), (d) EDS analysis results

The secondary phases at the grain boundaries were also characterized by SEM/TEM/EDS. As shown in Fig. 4(a), a phase with brighter contrast than Al_2Cu is distributed along the boundaries. EDS analysis (Figs. 4(b) and 4(c)) confirms that this phase is distinct from the intragranular $Al_{20}Ti_2Ce$ and can be identified as $Al_{16}Cu_4Mn_2Ce$, consistent with prior reports[19]. These results indicate that the solidification of the Ce-containing alloy involves a complex eutectic reaction: $L \rightarrow Al + Al_2Cu + Al_{16}Cu_4Mn_2Ce$.

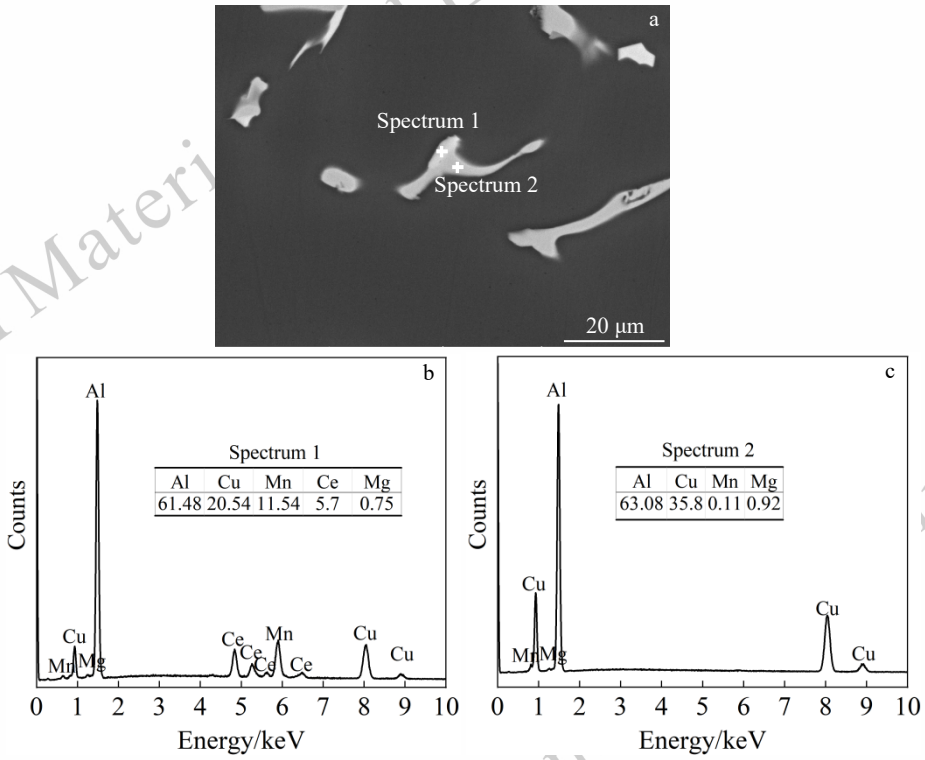

Fig. 4 Typical second phase at the grain boundary of as-cast 0.3Ce alloy: (a) back-scattered electron image; (b), (c) EDS analysis results

The grain boundary phase was further analyzed by TEM-EDS. As shown in Fig. 5, EDS identifies the strip-like particle as $Al_{16}Cu_4Mn_2Ce$. The corresponding SAED patterns (Figs. 5(c, d)) were acquired from this phase. The hexagonal symmetry of the diffraction spots in Fig. 5(c) is consistent with an face-centered cubic (FCC), hexagonal close-packed (HCP) or body-centered cubic (BCC) structure. Indexing of both patterns confirms an FCC structure for $Al_{16}Cu_4Mn_2Ce$, with the patterns corresponding to the $[\bar{1}11]$ and $[\bar{2}23]$ zone axes, respectively. A detailed analysis of its crystal structure is beyond the scope of this study and will be presented elsewhere.

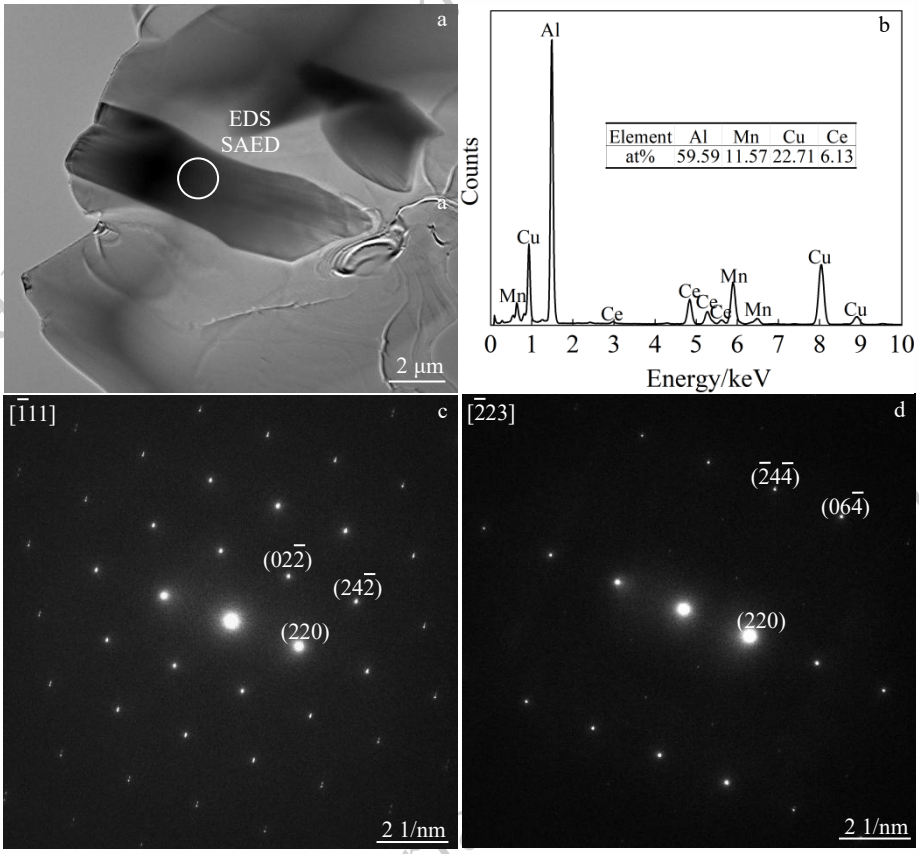

Fig. 5 Strip-like phase in the as-cast 0.3Ce alloy: (a) bright field image; (b) EDS result; (c), (d) SAED patterns

2.3 Phase transformation

Fig. 6 shows the microstructure and corresponding EDS analysis of the heat-treated 0.3Ce sample. The results confirm that the blocky/needle-like phase remains $Al_{20}Ti_2Ce$, with its morphology and composition showing negligible alteration after heat treatment. This observation is consistent with previous reports[19], further confirming the exceptional high thermal stability of this intermetallic phase, showing almost no dissolution and negligible morphological change during the 525 °C solution treatment applied in this study.

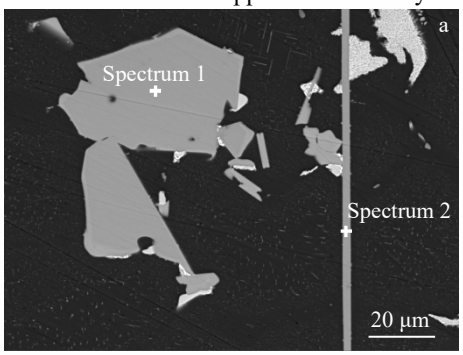

b

EDS results (at%)

Elements	Al	Ti	Ce	Mg	Cu
Spectrum 1	73.47	15.13	8.29	1.43	1.68
Spectrum 2	74.94	14.27	7.82	1.45	1.52

Fig. 6 Block/needle-like phase in heat-treated 0.3Ce sample: (a) back-scattered electron image; (b), (c) EDS analysis results

Fig. 7(a) shows the grain boundary secondary phases in the heat-treated 0.3Ce alloy. Unlike the strip-like $Al_{16}Cu_4Mn_2Ce$ observed in as-cast alloy, these particles exhibit a distinct reticular morphology. However, EDS analysis (Fig. 7d) confirms that their composition remains consistent with $Al_{16}Cu_4Mn_2Ce$. Moreover, internal contrast variations within the particles are evident. These features collectively suggest that the $Al_{16}Cu_4Mn_2Ce$ phase has undergone a transformation during heat treatment, despite retaining its nominal chemical composition.

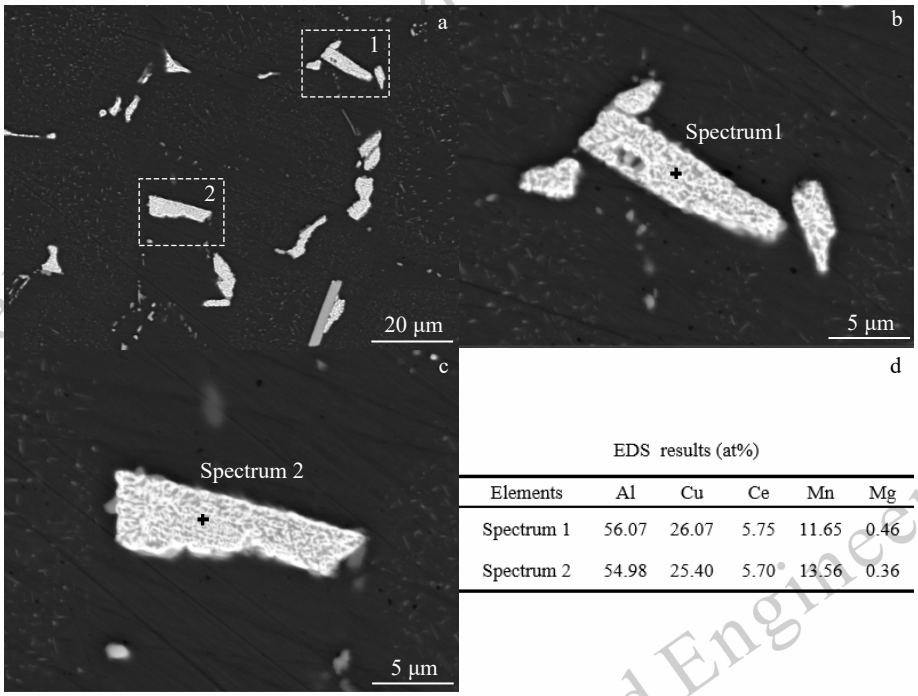

EDS results (at%)

Elements	Al	Cu	Ce	Mn	Mg
Spectrum 1	56.07	26.07	5.75	11.65	0.46
Spectrum 2	54.98	25.40	5.70	13.56	0.36

Fig. 7 The second phase at the grain boundaries in heat-treated 0.3Ce alloy: (a) back-scattered electron image; (b), (c) enlarged images of the selected area 1 and 2 in (a); (d) EDS results of the second phase

TEM analysis was employed to investigate the phase transformation of $Al_{16}Cu_4Mn_2Ce$ during heat treatment (Fig. 8). EDS mapping reveals two distinct phases within the observed region. In the HAADF image, the bright particles are enriched in Ce and Cu, along with some Mg and Mn. In contrast, the dark particles are rich in Mn and Cu but contain no Ce.

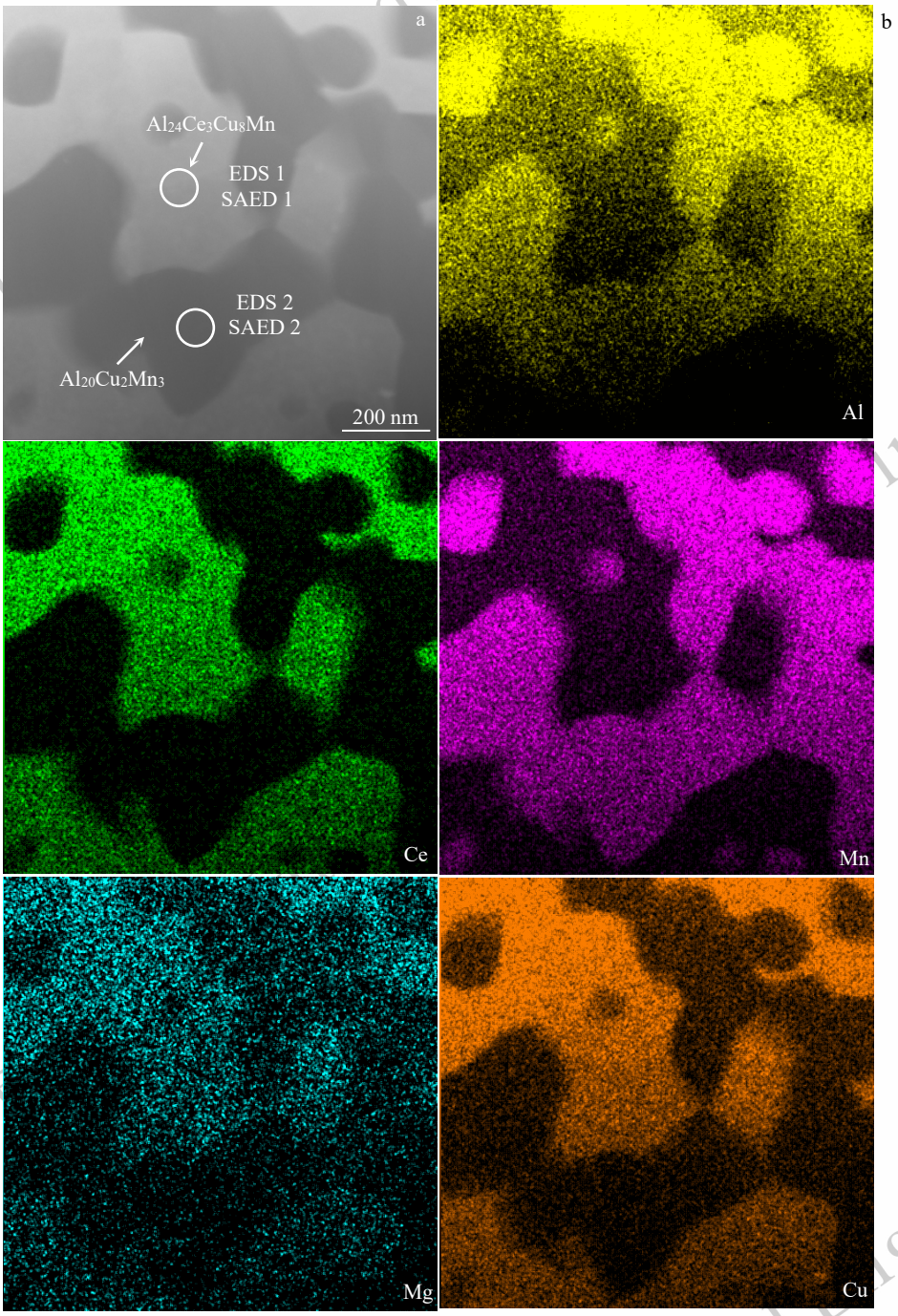

Fig. 8 The EDS mapping of the second phase in heat-treated 0.3Ce alloy

The two phases were analyzed by SAED and EDX, with results shown in Figs. 9(a)-(c). Based on the combined SAED patterns and EDX compositional measurements, the bright and dark particles are identified as $Al_{24}Ce_3Cu_8Mn$ and $Al_{20}Cu_2Mn_3$ (T phase), respectively. This confirms that the $Al_{16}Cu_4Mn_2Ce$ phase formed during solidification is metastable and transforms into $Al_{24}Ce_3Cu_8Mn$ and T phases during heat treatment.

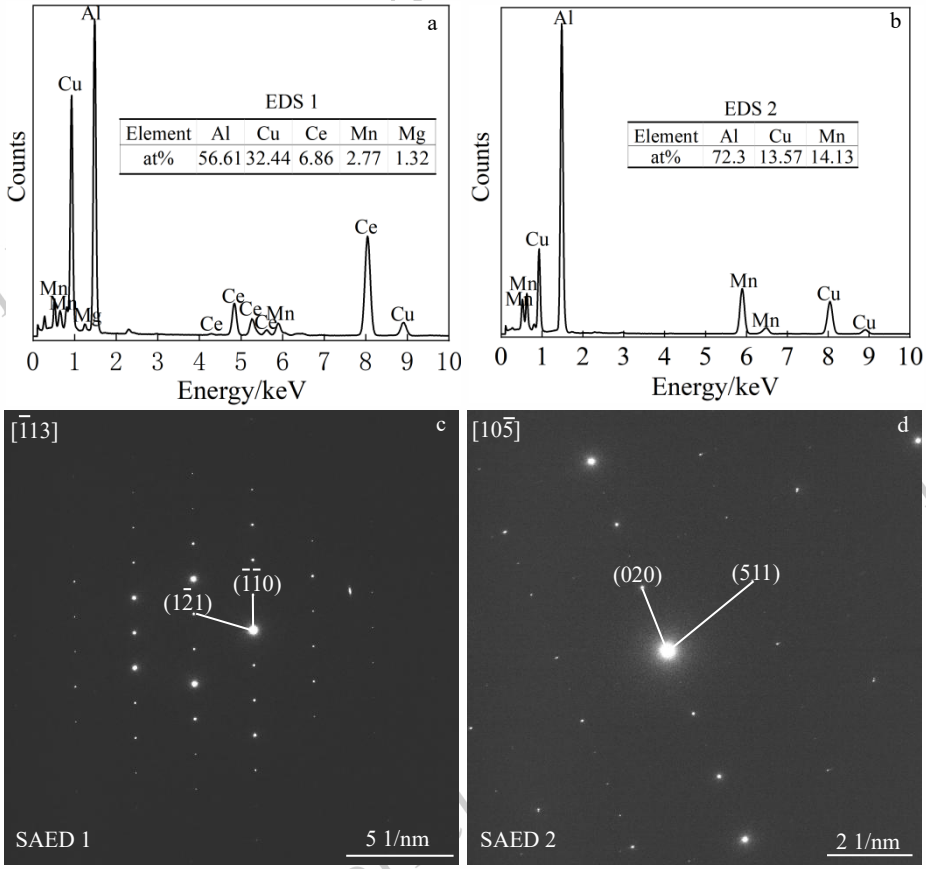

Fig. 9 The EDS results and SAED patterns of two positions in Fig. 8: (a), (c) position 1, (b), (d) position 2

2.4 Mechanical properties

Fig. 10 shows the engineering stress-strain curves of Al-Cu-Mn-Mg alloy with different Ce contents at room temperature, respectively, the mechanical properties are listed in Table 2. Ce microalloying significantly degrades both the strength and plasticity. Specifically, with Ce content increasing from 0 to 0.3wt.%, the yield strength (YS), ultimate tensile strength (UTS), and elongation (EL) decrease from 343 ± 3 MPa, 468 ± 7 MPa, and 7 ± 1% to 297.5 ± 6.5 MPa, 373 ± 15 MPa, and 3 ± 1%, respectively. At the lower Ce content (0.1 wt.%), the UTS shows a moderate decrease, while the YS drops dramatically, indicating a reduced strengthening contribution from minor Ce addition. According to the analysis, this is partly due to the formation of Ce-containing compounds ($Al_{16}Cu_4Mn_2Ce$ in the as-cast state, and $Al_{24}Ce_3Cu_8Mn$ and $Al_{20}Cu_2Mn_3$ after heat treatment), which reduces the supersaturation of Cu and Mn near the grain boundaries. This depletion impairs the precipitation of strengthening phases during heat treatment, resulting in a lower precipitate density around the eutectic regions and consequently a decrease in yield strength compared to the Ce-free alloy. As the Ce content increases from 0.1% to 0.2%, the YS remains nearly constant, suggesting that the effect of Ce alloying on strengthening tends to stabilize.

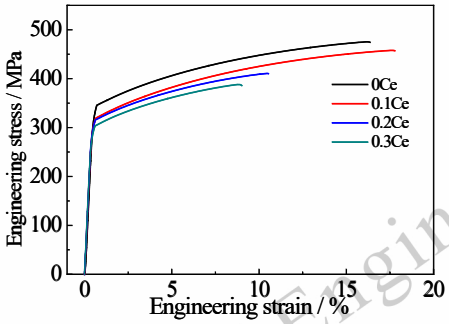

Fig.10 The stress-strain curves of alloys

Table 2 The room temperature mechanical results

Ce（%）	UTS (MPa)	YS (MPa)	EL (%)
0	468±7	343±3	7±1
0.1	453±5	319.5±1.5	8±1
0.2	408±3	311±4	4.5±2.5
0.3	373±15	297.5±6.5	3±1

The fracture surfaces of the alloys with different Ce contents are shown in Fig. 11. The Ce-free alloy exhibits numerous fine ductile dimples, indicative of substantial plastic de-

formation. With the addition of 0.1wt.% Ce, the area fraction of ductile dimples decreases. This is because the grain boundary eutectic ($Al_{24}Ce_3Cu_8Mn$ and $Al_{20}Cu_2Mn_3$) formed during heat treatment provides preferential sites for fracture initiation. Notably, no $Al_{20}Ti_2Ce$ particles are observed on this fracture surface. When the Ce content reaches 0.2 wt.%, blocky $Al_{20}Ti_2Ce$ particles become visible on the fracture surface, accompanied by clear cleavage facets. As $Al_{20}Ti_2Ce$ is a brittle intermetallic, it readily initiates cracks during tensile testing, which accounts for the continued decrease in elongation with increasing Ce content.

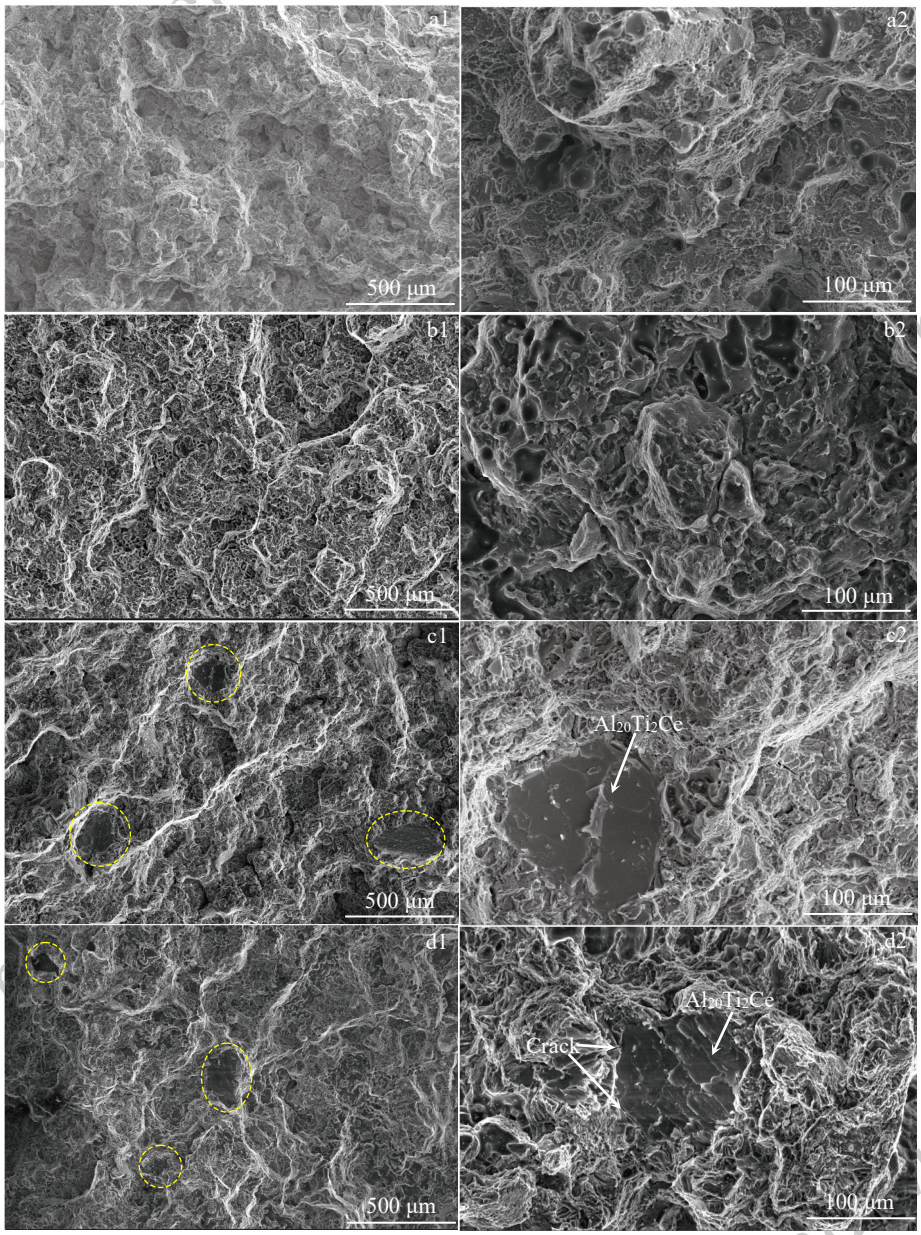

Fig. 11 Secondary electron images of the tensile fracture surfaces: (a1)、(a2) 0Ce alloy; (b1)、(b2) 0.1Ce alloy; (c1)、(c2) 0.2Ce alloy; (d1)、(d2) 0.3Ce alloy

To elucidate the marked decline in yield strength, the key strengthening precipitates in the alloys were characterized. In precipitation-hardened Al-Cu alloys, room-temperature strength is predominantly governed by the characteristics of age-hardening precipitates, including their type, size and volume fraction. The differences in mechanical strength among the experimental alloys (Fig. 10) can be effectively interpreted using an established strength model[20].

The 0.2Ce alloy is taken as representative of the Ce-containing alloys. Bright-field TEM images and corresponding SAED patterns of the heat-treated 0Ce and 0.2Ce alloys are shown in Fig. 12. The microstructure of the 0Ce alloy is dominated by θ′ precipitates[21], as confirmed by the characteristic diffraction spots indicated by arrows in Fig. 12b.

In contrast, the SAED pattern of the 0.2Ce alloy (Fig. 12d) exhibits discontinuous streaks along $(200)_{\alpha}$ with intensity maxima at the ¼, ½, and ¾ positions, identifying θ″ as the primary precipitate. These results demonstrate that the addition of minor Ce retards the θ″ → θ′ transformation, leading to different dominant precipitates in the two alloys despite identical heat treatment.

To quantify the strengthening contribution of θ″/θ′ precipitates, their diameter and thickness distributions were statistically analyzed, as shown in Fig. 13. The 0.2Ce alloy exhibits significantly finer precipitates, with an average diameter of (33.2 ± 1.3) nm and thickness of (1.799 ± 0.044) nm. In contrast, the precipitates in the 0Ce alloy are considerably coarser, averaging (109.9 ± 5.1) nm in diameter and (4.679 ± 0.272) nm in thickness. Additional quantitative TEM data are summarized in Table 2.

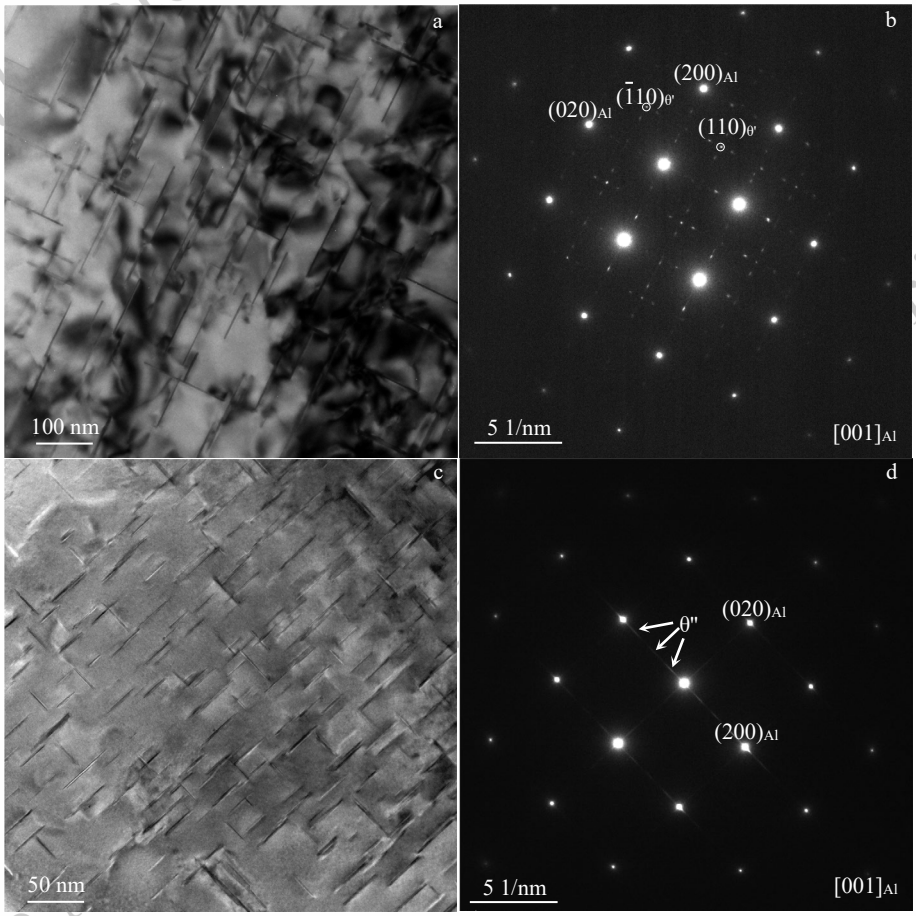

Fig. 12 Bright-field TEM images (a, b) and corresponding SAED patterns (c, d) viewed along $<001>_{\alpha\text{-Al}}$: (a, b) 0Ce alloy, (c, d) 0.2Ce alloy

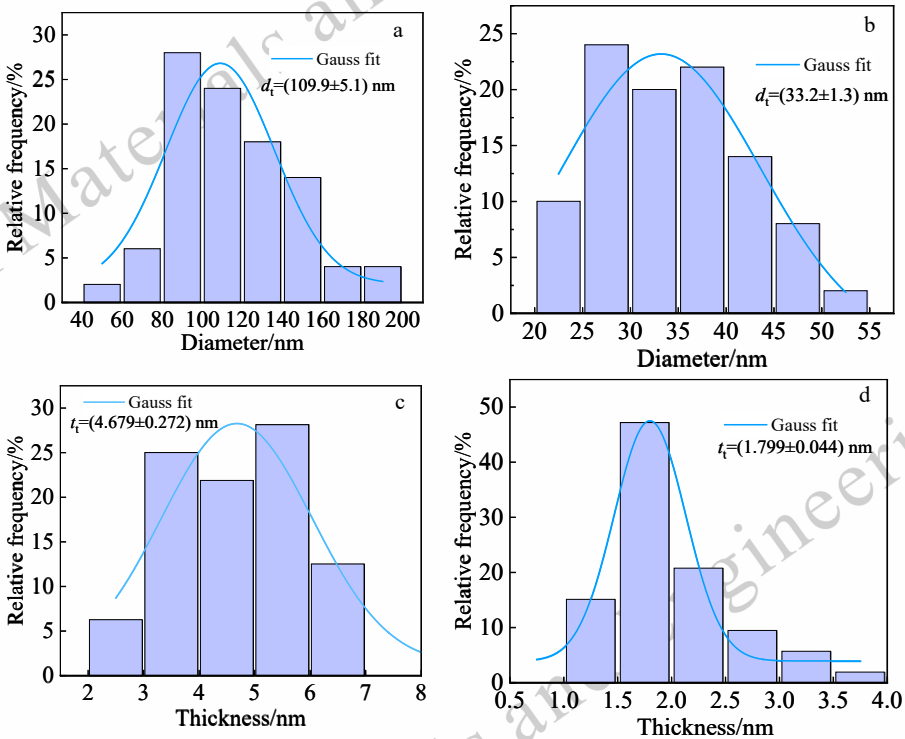

Fig. 13 Distribution of diameters (a, b) and thickness (c, d) of θ′/θ″ phases in 0Ce (a, c) and 0.2 Ce (b, d) alloys at T6 state

The θ" phase enhances alloy strength through multiple mechanisms including interfacial strengthening, coherency strengthening, and modulus mismatch strengthening, all of which originate from the interactions between the precipitates and dislocations[22, 23]. It is well established that a higher volume fraction of θ" precipitates leads to a significant increase in strength. Due to their coherency with the α-Al matrix and their shearable nature, θ" precipitates contribute primarily through coherency strengthening and interfacial strengthening. In contrast, the effects of modulus mismatch strengthening and order strengthening are generally considered negligible[22, 24]. The contribution of the θ" precipitates to the critically resolved shear stress (CRSS), $\Delta\tau$, due to coherency strengthening can be estimated as follows[25].

$$\Delta\tau = 4.1 \cdot G \cdot \left|\varepsilon^{3/2}\right| \cdot \left[\frac{f\, d_t}{2b}\right]^{\frac{1}{2}} \quad (1)$$

where G is the shear modulus of the α-Al matrix (28 GPa [25]), ε is the lattice strain (0.006 [24]), f is the volume fraction of precipitates, b is the magnitude of the Burgers vector for aluminum (0.284 nm [24]), and d_t is the effective width of the θ" precipitates.

The increase in the CRSS due to interfacial strengthening of the θ" phase results from the formation of new interfaces during its interactions with dislocations[22, 24] and can be estimated as[22].

$$\Delta\tau = \left(\frac{0.908 d_t}{t_t^2}\right)\left(\frac{bf}{\Gamma}\right)^{\frac{1}{2}} \gamma_i^{\frac{3}{2}} \quad (2)$$

where t_t is the effective thickness of the θ" precipitates;γ_i is the interfacial energy (0.21 J/m^2 [17]), and Γ represents the dislocation line tension, which is expressed as.

$$\Gamma = \frac{Gb^2}{2\pi} \ln \sqrt{\frac{d_t^2}{2b^2 f}} \quad (3)$$

The CRSS increments due to coherency and interfacial strengthening by the θ" precipitates in the 0.2Ce alloy are calculated as 50.6 and 38.8 MPa, respectively. The YS increment due to precipitates, σ_p, is obtained as.

$$\sigma_p = M \cdot \Delta\tau \quad (4)$$

Where M is the Taylor factor (M=3[24]). As shown in Table 2, the σ_p value of 0.2Ce alloy is estimated to be 268.2 MPa, which accounts for ~86% of the experimentally measured YS. This suggests reasonable agreement between the estimated YS increment due to θ" pecipitates and the measured YS, because the strengthening effects of other mechanisms, such as solid solution hardening and grain size hardening in the T6-treated alloys, remain relatively low.

Furthermore, the θ' particles formed in the 0Ce alloy are non-shearable; therefore, they contribute to alloy strengthen-

ing via the Orowan looping mechanism[24]. The CRSS increment due to θ' particles with the observed characteristics (Table 2) is estimated as[20]

$$\Delta\tau = \left(\frac{Gb}{2\pi\sqrt{1-\nu}}\right)\left(\frac{1}{1.23\frac{1.03}{\sqrt{N_v d_t}} - \frac{\pi d_t}{8} - 1.061 t_t}\right)\left(\ln\frac{0.981\sqrt{d_t t_t}}{b}\right) \quad (5)$$

Where N_v is the number density of θ' precipitates, and ν is the Poisson ratio (0.33 for face-centered cubic metals[20]). The YS increments due to θ' particles in the 0Ce alloy is estimated to be 325.2 MPa, which confirms that the θ' precipitates observed in the 0Ce alloy make a much larger contribution to strengthening of the alloy than θ'' precipitates observed in the 0.2Ce alloy (Table 2). Therefore, the reduction in yield strength shown in Fig. 10 can be primarily attributed to the modification of the strengthening phase induced by the addition of Ce. In other words, under identical heat-treatment conditions, the 0Ce alloy reaches peak-aged hardness at 175 ℃ for 6 h and the Ce-containing alloys will not because the addition of Ce can retard the transformation from θ'' to θ'.

To verify that Ce retards the θ''→θ' transformation, the hardness-aging time curves for the 0Ce and 0.2Ce alloys are plotted in Fig. 14 (microhardness measured in the α-Al matrix). As shown, the peak hardness occurs at 6 h for the 0Ce alloy and at 8 h for the 0.2Ce alloy. Moreover, the 0Ce alloy exhibits a higher peak-aged hardness (147.4 ± 1.2 HV) than the 0.2Ce alloy (144.5 ± 1.7 HV).

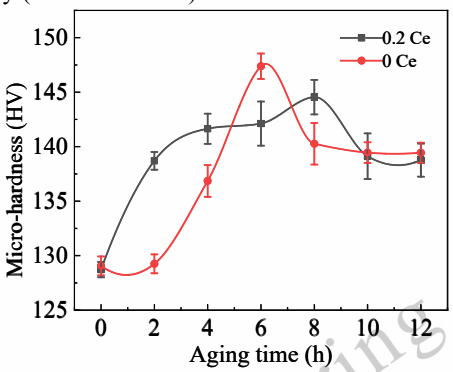

Fig. 14 The age hardening curves of 0Ce and 0.2Ce alloys aged at 175 ℃ for different times

Table 2 Summary of quantitative TEM results of θ′′ and θ′ phase characteristics in 0Ce and 0.2Ce alloys under T6 conditions.

Alloy	Phase	Mean diameter, d_t/nm	Thickness, t_t/nm	Number density, N_v/μm^{-3}	Volume fraction, f/%	Δτ, MPa	σ_p, MPa
0Ce	θ′	109.9±5.1	4.679±0.272	1200.0	0.0532	108.4	325.2
0.2Ce	θ′′	33.2±1.3	1.799±0.044	9877.6	0.0154	89.4	268.2

Furthermore, the effect of grain size on mechanical properties the 0Ce and 0.2Ce alloys has been also analyzed. The yield strength, σ_p, is dependent on the average grain boundary diameter (D) by Hall-Petch relationship.

$$\sigma_p = \sigma_0 + kD^{-1/2} \quad (5)$$

where σ_0 is the intrinsic resistance of the lattice to dislocation motion, and k is the constant representing the relative strengthening contribution from grain boundaries. For Al alloys, k is usually taken to be 0.14 MN/m$^{3/2}$. According to the Hall-Petch equation, the theoretical decrease in yield strength due to grain coarsening from 136 μm to 231 μm is only ~2.8 MPa[27]. This suggests that the influence of grain size variation on the mechanical properties of alloys is negligible.

3 Conclusions

1) Primary $Al_{20}Ti_2Ce$ and eutectic $Al_{16}Cu_4Mn_2Ce$ phase can be formed during the solidification when Ce element is added into Al-Cu-Mn-Mg alloy. The volume fraction of these Ce-containing quaternary compounds increases with increasing Ce content.

2) $Al_{20}Ti_2Ce$ is highly stable and its morphology remains unchanged during heat treatment. In contrast, $Al_{16}Cu_4Mn_2Ce$ is unstable, this eutectic phase transforms into $Al_{24}Ce_3Cu_8Mn$ and $Al_{20}Cu_2Mn_3$ during heat treatment.

3) The addition of minor Ce retards the phase transformation from θ'' to θ' in the Al matrix. As the Ce content increases from 0 to 0.3 wt.%, the mechanical properties of the alloys deteriorate: the ultimate tensile strength and yield strength decrease by 95 MPa and 45.5 MPa, respectively, and the elongation decreases by about 50% compared with those of the Ce-free base alloy.

References

[1] J. U. Rakhmonov, S. Bahl, A. Shyam *et al. Acta Materialia*[J], 2022, 228.

[2] Fan Zhang, Dongjin Shi, Ziyu He *et al. Journal of Materials Research and Technology*[J], 2023, 25: 2815-2825.

[3] Guodong Niu, Langjie Zhu, Wangrui Ren *et al. Materials Characterization*[J], 2023, 200: 112908.

[4] F. Theska, Y. Yang, K. D. Sisco *et al. Materials Characterization*[J], 2022, 191: 112109.

[5] Wei Tian, Mengnan Hu, Xiaohong Chen *et al. Materials Research Express*[J], 2020, 7(3): 36532.

[6] Binbin Zhao, Yongzhong Zhan, HongqunTang. *Materials Science and Engineering: A*[J], 2019, 758:7-18.

[7] Jiandi Du, Dongyan Ding, Wenlong Zhang *et al*. *Materials Characterization*[J], 2018, 142: 252-260.
[8] Ming Li, HongweiWang, Zunjie Wei *et al*. *Materials and Design*[J], 2010, 31: 2483-2487.
[9] D. H. Xiao, J. N. Wang, D. Y. Ding *et al*. *Journal of Alloys and Compounds*[J], 2003, 352(1): 84-88.
[10] Min Song, Daihong, Xiao, Fuqin Zhang. *Rare Metals*[J], 2009, 28(2): 156-159.
[11] Yuntao Li, Zhiyi Liu, Jie Zhou *et al*. *Transactions of Nonferrous Metals Society of China*[J], 2007, 17(A01): 266-270.
[12] D. H. Xiao, J. N. Wang, D. Y. Ding. *Materials Science and Technology*[J], 2004, 20(10): 1237-1240.
[13] Min Song, Kanghua Chen, Lanping Huang. *Rare Metals*[J], 2007,26(1):28-32.
[14] Zhao H L, Guan R G, Li M *et al*. *Journal of Central South University*[J], 2014, 21(1): 1-8.
[15] Liang Meng, Xiulin Zheng, Li Tian. *Materials science & engineering. A*[J], 1995, 196(1): 191-196.
[16] Zhongwei Chen, Pei Chen, Shishun Li. *Materials Science and Engineering: A*[J], 2012, 532: 606-609.
[17] Yadong. Lv, Han Zhang, Qitang Hao *et al*. *Materials Today Communications*[J], 2025, 42.
[18] Han Zhang, Qitang Hao, Xinlei. Li *et al*. *Nanomaterials*[J], 2023,13(23).
[19] Xiang Su, Hongjie Qu, Yuan Lei *et al*. *Crystals*[J], 2023, 13(3): 380.
[20] S. Roy, L. F. Allard, A. Rodriguez *et al*. *Metallurgical and materials transactions. A*[J], 2017, 48(5): 2543-2562.
[21] Zhenju Shen, Qingqing Ding, Chunhui Liu *et al*. *Journal of Materials Science & Technology*[J], 2017, 33(10): 1159-1164.
[22] J. F. Nie, B. C. Muddle. *Journal of Phase Equilibria*[J], 1998, 19(6): 543-551.
[23] Yiqiang Chen, Zezhong Zhang, Zhen Chen *et al*. *Acta Materialia*[J], 2017, 125: 340-350.
[24] S. Mondol, S. K. Makineni, S. Kumar *et al*. *Metallurgical and Materials Transactions. A*[J], 2018, 49(7): 3047-3057.
[25] L. M. Brown, R. K. Ham. Strengthening Methods in Crystals[M]. New York: Wiley, 1971.
[26] O. Engler, C. D. Marioara, Y. Aruga *et al*. *Materials Science and Engineering. A*[J], 2019, 759: 520-529.
[27] Ruidi Li, MinboWang, Zhiming Li *et al*. *Acta Materialia*[J], 2020, 193: 83-98.

稀土元素 Ce 对 Al-Cu-Mn-Mg 合金显微组织及力学性能的影响

余文涛[1,2]，张晗[3]，张卫霞[4]，吕亚东[2]，杨海燕[2]，薛彦庆[4]，郝启堂[2]

(1. 西安文理学院 机械与材料工程学院，陕西 西安 710065)

(2. 西安文理学院 陕西省表面工程与再制造重点实验室，陕西 西安 710065)

(3. 西北工业大学 凝固技术全国重点实验室，陕西 西安 710072)

(4. 陕西有色天策新材料科技有限公司，陕西 西安 710100)

(5. 西安邮电大学，陕西 西安 710121)

摘 要：采用光学显微镜（OM）、扫描电镜（SEM）、透射电镜（TEM）及 X 射线衍射（XRD）等表征技术研究了微量 Ce 对 Al-Cu-Mn-Mg 合金显微组织与力学性能的影响。结果表明：随着 Ce 含量的增加，合金中会形成两种不同的含 Ce 化合物，一种是凝固过程中形成的初生 $Al_{20}Ti_2Ce$ 相，该相的出现消耗了铝熔体中有效的晶粒细化元素 Ti，导致合金的晶粒粗化。另一种是凝固后期通过共晶反应形成的 $Al_{16}Cu_4Mn_2Ce$ 相，该相在高温下不稳定，热处理过程中会转变为 $Al_{24}Ce_3Cu_8Mn$ 和 $Al_{20}Cu_2Mn_3$，无法使 $Al_{16}Cu_4Mn_2Ce$ 相中的 Cu、Mn 元素固溶进入 Al 基体，导致热处理后合金基体中 Cu、Mn 元素的过饱和度下降。此外，Ce 的添加会延缓铝基体中 θ"相向 θ'相的转变过程，同等热处理条件下，含 Ce 合金 Al 基体中的主要强化相为 θ"，而 0Ce 合金中为 θ'。稀土元素 Ce 对合金相组成及显微组织的影响直接体现在合金力学性能的变化，当 Ce 含量由 0 增加至 0.3 wt%时，与不含 Ce 的基础合金相比，0.3Ce 合金的抗拉强度和屈服强度分别下降了 95 MPa 和 45.5 MPa，伸长率下降了约 50%。

关键词：Al-Cu-Mn-Mg合金；Ce；显微组织；力学性能

作者简介：余文涛，男，1983 年生，博士，高级讲师，西安文理学院 机械与材料工程学院，陕西 西安 710065，E-mail: yuwentao417@xawl.edu.cn